

Passive control of the flow around a hemisphere using porous media



C. Mimeau^a, I. Mortazavi^{a,*}, G.-H. Cottet^b

^a EA-7340-M2N-Modélisation, Mathématique et Numérique, Conservatoire National des Arts et Métiers, 2 Rue Conté, 75003 Paris, France

^b Univ. Grenoble-Alpes, LJK, 51 rue des Mathématiques, F-38041 Grenoble, France

ARTICLE INFO

Article history:

Received 21 December 2015

Received in revised form

31 January 2017

Accepted 2 March 2017

Available online 12 April 2017

Keywords:

Passive flow control

Porous media

Drag reduction

Flow past a hemisphere

Vortex methods

Brinkman penalization method

ABSTRACT

In this work, a passive flow control study is proposed in order to regularize the flow dynamics around a hemisphere at a low and a higher Reynolds number in the wake transition regime. This passive control is realized by covering the projected curved surface of the hemisphere with a porous coating. The presence of such porous medium modifies the boundary conditions at the body–fluid interface, allowing a non-zero velocity to settle in this region. This phenomenon smoothes the global flow dynamics and leads, in particular, to a decrease of the energy dissipation and the aerodynamic force. In this paper, the flow control study is carried out for several configurations using a vortex-penalization technique which allows to easily model solid–fluid–porous media without prescribing any boundary condition.

© 2017 Elsevier Masson SAS. All rights reserved.

1. Introduction

The main advantage of passive control for drag reduction, in aerodynamics, relies in the fact that it is energy free and generally easy to implement. Many devices have been proposed in the literature as for instance compliant walls like the dolphin skin [1,2], riblets or bumps [3–5], and wavy or rough surfaces [6,7]. Another possibility is to introduce porous and permeable layers [8]. The main effect of a porous interface between the solid and the fluid is to change the shear forces. Indeed, the no-slip boundary condition is replaced by a quasi-slip boundary condition [9] due to the Darcy flow inside the porous layer; as a result, the rate of vorticity generation is reduced. Therefore the shedding around a bluff body is modified and the flow behavior can be drastically regularized. The efficiency of this passive control is related to the choice of the permeability of the porous medium, the thickness of the porous layers and their location. As highlighted in [10], it is interesting to mention that flow throughout porous (or porous-like) media may be observed in multiple applications, like tennis balls [11] or carbon-nanotubes-based flow sensors [12], as well as natural structures like vegetation canopies [13], birds' covert feathers [14] or endothelial glycocalyx (i.e. “sweet shield”) of blood vessels [15]. The presence of such porous devices enables a damping

of the flow-induced surface instabilities, therefore modifying the flow behavior in the vicinity of the solid–porous–fluid interface.

In this paper, passive control is explored to regularize three-dimensional flows around a hemisphere and more specifically to reduce the drag forces, and focuses on the physics of these underlying flows. The main reason for choosing the hemisphere geometry is its similarity to the side view mirrors of a ground vehicle and the possible extension of this control to reduce their drag. Indeed, in spite of the fact that the mirrors only represent 0.5% of the projected surface of the vehicle, they are responsible for about 10% of the total aerodynamic drag because of their spanwise position. Moreover, due to the size and the geometry of side view mirrors, passive control devices appear as the most adapted. The passive manipulation considered here in order to smooth the flow dynamics involves porous media. Based on the works of [8,16,17], the control devices designed in the present work rely in a total or partial coating of the hemisphere surface with a porous layer. Under optimal conditions related to the permeability of the added porous layer, its thickness and its position, the modifications of the flow induced by the presence of such device may lead to a regularization of the wake and to a drag reduction. In the previous related study performed for two-dimensional flows [18], the presence of a porous layer at the surface of a two-dimensional semi-circular cylinder was actually shown to be responsible for a decrease of the shear forces and the vorticity generation of the boundary layer, leading to aerodynamic improvements like drag reduction.

Regarding the numerical approach, we propose here a three-dimensional vortex-penalization method to approximate the incompressible flows in solid–fluid–porous media. Vortex methods

* Corresponding author.

E-mail address: iraj.mortazavi@cnam.fr (I. Mortazavi).

and immersed boundary methods have been separately used to simulate viscous recirculating flows around obstacles. The vortex-penalization method combines the advantages of both approaches. This technique maintains the efficiency and the robustness of vortex methods that solve the flow equations in a fast Lagrangian way [19,20]. On the other hand, the use of the Brinkman penalization technique [21,22] enables to simplify the treatment of the no-slip boundary conditions. This immersed boundary method consists in extending the fluid velocity inside the solid body and to solve the Navier–Stokes equations with a penalization term, depending on the intrinsic permeability, to enforce rigid motion inside the solid using a vorticity formulation [23]. The penalization technique can therefore be defined as an immersed boundary method based on permeability variations. The distinction between the three different media is indeed easily performed defining the value of the penalization parameter without prescribing a boundary condition at the solid boundary or a condition at the porous–fluid interface. Hence, it appears as a suitable approach to handle flows in solid–fluid–porous media and to perform passive flow control using porous interfaces.

In this work, the numerical method is first presented and then validated for three-dimensional viscous incompressible flows past bluff bodies for transitional Reynolds numbers. The application to passive flow control past a 3D hemisphere is finally proposed by adding a porous sheath on the obstacle surface in order to reduce the drag forces. This control study takes into account several configurations of the added porous layer around the hemisphere, involving different geometries, permeabilities and thicknesses. The flow physics is observed in detail for each of these configurations to better understand the control effects.

2. Hybrid vortex penalization method for solid–porous–fluid media

2.1. The governing equations

In this work, we use the so called Brinkman–Navier–Stokes equations in their velocity(\mathbf{u})–vorticity($\boldsymbol{\omega}$) formulation in order to model incompressible flows past obstacles. In three dimensions, these equations read as follows:

$$\frac{\partial \boldsymbol{\omega}}{\partial t} + (\mathbf{u} \cdot \nabla) \boldsymbol{\omega} - \text{div}(\boldsymbol{\omega} : \mathbf{u}) = \frac{1}{Re} \Delta \boldsymbol{\omega} + \nabla \times [\lambda \chi_S (\mathbf{u}_s - \mathbf{u})], \quad (1)$$

$$\Delta \mathbf{u} = -\nabla \times \boldsymbol{\omega}. \quad (2)$$

One can denote in Eq. (1) the advection term $(\mathbf{u} \cdot \nabla) \boldsymbol{\omega}$, the stretching term $\text{div}(\boldsymbol{\omega} : \mathbf{u})$ expressed in its conservative form, the diffusion term $\Delta \boldsymbol{\omega}/Re$ and the penalization term $\nabla \times [\lambda \chi_S (\mathbf{u}_s - \mathbf{u})]$. The Poisson equation (Eq. (2)) allows to recover the velocity field \mathbf{u} from the vorticity field $\boldsymbol{\omega}$ which has been convected, diffused and penalized through Eq. (1). Concerning the penalization term, it enables to model the presence of a solid body in the flow, varying the permeability of the medium. In this penalization term, χ_S denotes the characteristic function that yields 0 in the fluid and 1 in the solid, \mathbf{u}_s indicates the rigid body velocity which is zero in all this work since the body is fixed and $\lambda = \mu \Phi l_{ref} / \rho k u_{ref}$ is the non-dimensional penalization parameter essentially depending, in the inverse proportion, on the permeability k of the medium (with μ the viscosity, Φ the porosity of the porous material which is close to 1 as imposed by Brinkman equations, l_{ref} the height of the obstacle, ρ the fluid density and $u_{ref} = u_\infty$ the reference far field velocity). Varying the λ value thus directly defines the different media. Indeed, in the fluid, the intrinsic permeability coefficient k goes to infinity, thus λ tends to 0 in this region and we naturally recover the \mathbf{u} – $\boldsymbol{\omega}$ Navier–Stokes equations. On the contrary, the solid has a permeability coefficient k which goes to zero, it can be

consequently modeled setting the penalization parameter λ to a very high value. In our study λ equals 10^8 in the solid, which makes the flow velocity vanishing in this region. Furthermore, setting the λ parameter to an intermediate value, reasonably chosen between these two extreme values ($\lambda = 0$ and $\lambda = 10^8$), would model a porous medium in which the flow has a non-zero Darcy velocity \mathbf{u}_D . As a conclusion, the variation of λ corresponds to the variation of k that specifies the intrinsic porous material permeability.

2.2. Sketch of algorithm

To discretize the penalized vorticity equations (Eqs. (1), (2)) we use in this work a semi-Lagrangian vortex method. The flow is discretized into elements, also called particles, that carry the physical flow properties. The hybrid feature of the proposed method relies in its semi-Lagrangian framework. In practice, the resolution of the governing equations is based on a viscous splitting algorithm [24], which consists in the present context in successively solving at each time step the following equations:

$$\frac{\partial \boldsymbol{\omega}}{\partial t} = \nabla \times (\lambda \chi_S (\mathbf{u}_s - \mathbf{u})) \quad (3)$$

$$\frac{\partial \boldsymbol{\omega}}{\partial t} = \text{div}(\boldsymbol{\omega} : \mathbf{u}) \quad (4)$$

$$\frac{\partial \boldsymbol{\omega}}{\partial t} = \frac{1}{Re} \Delta \boldsymbol{\omega} \quad (5)$$

$$\frac{\partial \boldsymbol{\omega}}{\partial t} + (\mathbf{u} \cdot \nabla) \boldsymbol{\omega} = 0 \quad (6)$$

$$\Delta \mathbf{u} = -\nabla \times \boldsymbol{\omega}. \quad (7)$$

The penalization equation (Eq. (3)) is solved on a Cartesian grid using an implicit Euler scheme and the right hand side is evaluated by fourth order centered finite differences. Eq. (4) corresponds to the stretching equation with a conservative formulation of the stretching term, where $\text{div}(\boldsymbol{\omega} : \mathbf{u})$ is the vector of component $\frac{\partial(\omega_i u_j)}{\partial x_j}$. The space discretization of the stretching term is performed using a fourth order finite differences scheme for the derivatives. A RK3 scheme is used for time integration. Then, diffusion equation (Eq. (5)) is solved on the grid using FFT-based evaluations. Finally, the vorticity field is advected through Eq. (6) using a remeshed vortex method [19]: particles are pushed in a Lagrangian way with a RK2 time-stepping and are then redistributed on the original grid using a fourth order interpolation kernel [25,26]. Finally, the resulting velocity field is recovered from vorticity by solving the Poisson equation (7) on the grid with FFT-based evaluations. Grid values for vorticity and velocity are now available for time t_{n+1} and a new cycle of iterations can start. For a complete description of the present numerical method we refer the reader to the previous authors' work [27].

The no-slip boundary conditions are handled by penalizing the vorticity transport equations, through Eq. (3). Concerning far-field boundary conditions on the domain walls, we use periodic boundary conditions combined with correction techniques to ensure the proper inlet boundary conditions. In particular, this choice allows us to use the Fast Fourier Transform method in order to efficiently solve the Poisson equation $\Delta \mathbf{u} = -\nabla \times \boldsymbol{\omega}$. However, handling periodic boundary conditions implies special treatments on the flow fields in order to recover the desired uniform flow at the inlet $\mathbf{u}_\infty = (u_{ref}, 0, 0) = (1, 0, 0)$. These treatments appear in two types of corrections. First of all, one needs to discard the eddies coming periodically from the outlet. This is performed at each time step through a smooth absorption satisfying solenoidal vorticity on a narrow region at the outlet of the computational domain. In a second place, a correction has to be performed on the velocity

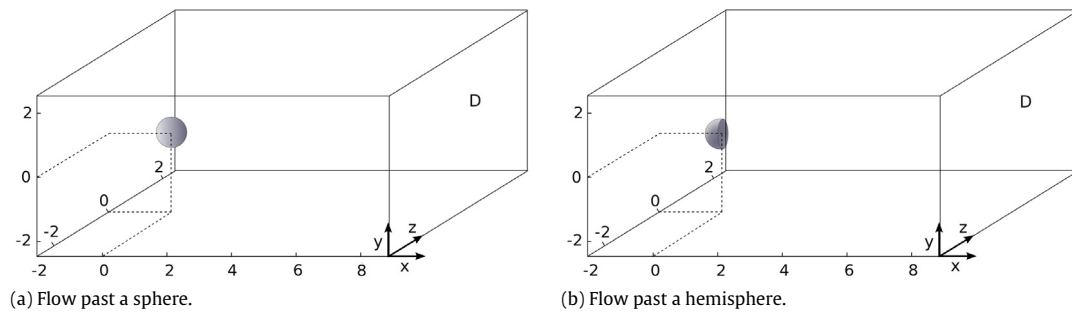


Fig. 1. Computational domain D .

field in order to recover the desired flux at the inlet and to account for a non-zero circulation. More details and validations concerning the treatment of the far-field boundary conditions may be found in [27]. This hybrid vortex penalization method has already been successfully used in 2D [28] and 3D [27] to simulate transitional and highly transitional flows past bluff bodies. In the following, we present additional validations for geometries corresponding to the physical configuration studied in this paper.

3. Validation results

In order to verify the accuracy of the method, we present in this section a validation study of the computational method employed in this work. For this purpose, we consider flows past a sphere and a hemisphere and we compare the results with the ones of the literature. Each simulation presented in the following is performed considering the same geometrical setup: the obstacle under study has a dimensionless diameter of $d = 1$ and its center (in the case of the sphere) or its back wall (in the case of the hemisphere) is located at $(x, y, z) = (0, 0, 0)$ in the computational domain $D = [-2, 8.48] \times [-2.56, 2.56] \times [-2.56, 2.56]$ (Fig. 1). The whole domain is meshed by an equispaced Cartesian orthogonal grid where particles are initialized and remeshed at every time step. Based on previous grid refinement studies [28,27], we set the grid step to $h = 0.02$ for simulations performed at $Re = 300$ and to $h = 0.01$ at $Re = 1000$. The penalization parameter is set to $\lambda = 10^8$ inside the body. The time step is adaptative and calculated at each iteration according to the Lagrangian CFL condition:

$$\Delta t_{\text{adapt}} = \frac{\text{LCFL}}{|\nabla \mathbf{u}|_{\infty}}, \quad (8)$$

where LCFL must be smaller than 1. In this work $\text{LCFL} = 1/8$.

3.1. Flow past a sphere

As concerns validation process, we first consider the classical benchmark of flow around a sphere at $Re = 300$. The 3D computational box D is meshed by a uniform $512 \times 256 \times 256$ Cartesian grid, which corresponds to a mesh size of $h = 0.02$. In the early times of the simulation, a perturbation is applied to the flow in order to trigger the instability. This perturbation is imposed between $T = 3$ and $T = 4$ on the y component of the velocity and stands as $u_{y\infty} = \sin(\pi(T - 3))$. Table 1 provides the values of the drag and vertical lift coefficients obtained with the present method, as well as the Strouhal number. These values are compared to several results of the literature and as the table shows, our results coincide well with the references.

The flow analysis at $Re = 1000$ is also considered. The simulation is performed on a uniform $1024 \times 512 \times 512$ Cartesian mesh ($h = 0.01$). A perturbation is defined in this case by $u_{y\infty} = 0.1 \sin(\pi(T - 3))$, between $T = 3$ and $T = 4$. A plot of the

Table 1
Comparison of drag and lift coefficients and Strouhal number for flow past a sphere at $Re = 300$.

| Authors | $Re = 300$ | | |
|------------------------------------|-------------|-------------|-------|
| | \bar{c}_D | \bar{c}_L | S_t |
| Roos & Willmarth ^a [29] | 0.629 | – | – |
| Johnson & Patel [30] | 0.656 | –0.069 | 0.137 |
| Tomboulides & Orszag [31] | 0.671 | – | 0.136 |
| Constantinescu & Squires [32] | 0.655 | –0.065 | 0.136 |
| Kim & Choi [33] | 0.657 | –0.067 | 0.134 |
| Ploumhans et al. [34] | 0.683 | –0.061 | 0.135 |
| Present work | 0.673 | –0.066 | 0.133 |

^a Refers to experimental results.

time average streamwise velocity u_x along the centerline is given in Fig. 2(a). The results obtained with the present method are compared to those of [31] together with the experimental data of [35] obtained at $Re = 960$. They show a good agreement. The same conclusion holds for the time evolution of force coefficients. Indeed, as shown in Fig. 2(b), the time evolution of the drag coefficient C_D and the vertical lift coefficient C_L coincide with the one found by [34]. The mean value of the drag coefficient C_D obtained from long time computations is 0.485, to be compared with the numerical values reported by [36] and [37], respectively equal to 0.46 and 0.478.

3.2. Flow past a hemisphere

It is important to validate the numerical method used in the present study for flows past a hemisphere. To our knowledge, the only study related to this problem is the numerical work of Kim and Choi [38], where an immersed boundary method in a cylindrical coordinate system is used to investigate the behavior of flows past a hemisphere at different Reynolds numbers, ranging from 100 to 300. In the present validation study we will focus on three values of the Reynolds number, corresponding to different unsteady flow behaviors: $Re = 200, 250$, and 300 . These Reynolds numbers are also studied in detail in [38]. For each simulation, the domain D is meshed with a $512 \times 256 \times 256$ Cartesian grid ($h = 0.02$). The hemisphere has a diameter d equal to 1 and its rear back surface is centered at the point $(0, 0, 0)$ (Fig. 1(b)). As we did for the sphere, the flow instability is triggered by a perturbation imposed between $T = 3$ and $T = 4$. The compared results are reported in Table 2. We notice that the results agree rather well with each other.

All these validation results therefore confirm the capability of the present semi-Lagrangian penalization method to accurately model incompressible bluff body flows.

4. Passive flow control past a 3D hemisphere

The vortex penalization method is now applied to passive flow control around a 3D hemisphere. The control is achieved covering the obstacle with a porous coating, without changing its original shape and size. The expected effect of a porous medium

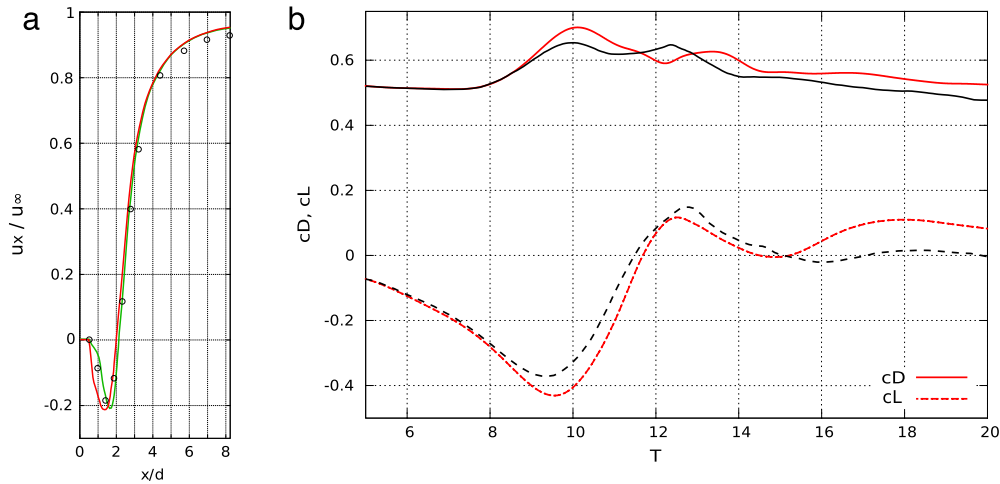


Fig. 2. Flow past a sphere at $Re = 1000$: (a) Average streamwise velocity u_x along the x -axis: comparison of the present results (red curve) with numerical results [31] (green curve) and experimental data [35] at $Re = 960$ (black circles). (b) c_D (solid lines) and c_L (dashed lines) time evolution: comparison of the present results (red curves) with [34] (black curves). (For interpretation of the references to color in this figure legend, the reader is referred to the web version of this article.)

Table 2

Comparison of mean drag and vertical lift coefficient as well as Strouhal numbers for flow past a hemisphere at $Re = 200, 250$ and 300 .

| $Re = 200$ | \bar{c}_D | \bar{c}_L | St_{lift} | St_{drag} |
|-----------------|-------------|--------------------|-------------|-------------|
| Kim & Choi [38] | 0.790 | 0.0 ± 0.024 | 0.128 | 0.256 |
| Present work | 0.805 | 0.003 ± 0.025 | 0.129 | 0.257 |
| $Re = 250$ | \bar{c}_D | \bar{c}_L | St_{lift} | St_{drag} |
| Kim & Choi [38] | 0.742 | 0.0 ± 0.05 | 0.127 | 0.254 |
| Present work | 0.757 | 0.0 ± 0.05 | 0.128 | 0.256 |
| $Re = 300$ | \bar{c}_D | \bar{c}_L | St_{lift} | St_{drag} |
| Kim & Choi [38] | 0.715 | 0.0 ± 0.062 | 0.135 | 0.270 |
| Present work | 0.729 | -0.002 ± 0.063 | 0.134 | 0.270 |

at the solid–fluid interface is to modify the vorticity generation of the boundary layer and the vortex shedding, and therefore to reduce drag forces, improving the aerodynamic properties of the obstacle [8,16,17]. In the following simulations, the hemisphere has a total dimensionless diameter of $d = 1$. This diameter includes a porous coating of thickness τ , constituting the passive control device. According to the Brinkman’s equation on which our model is based, the porosity Φ of the added coating has to be close to 1 (see Section 2.1). In practice, one can consider materials like wire crimps ($\Phi \sim 0.72$), fiberglass ($\Phi \sim 0.9$), steel wool ($\Phi \sim 0.9$) or hair like texture ($\Phi \sim 0.97$).

The two different Reynolds numbers considered in the present study are $Re = 300$ and $Re = 1000$. These choices correspond to the Reynolds numbers considered in our validation studies. These validations indeed enabled us to identify the mesh sizes allowing to account for the correct flow behaviors at these two Reynolds numbers, which correspond to two different flow regimes. Our goal is to give an accurate description and understanding of the physical mechanisms occurring in the presence of a porous medium, when all the time and space scales are resolved in a three-dimensional case. Although the values of the Reynolds numbers considered here do not correspond to realistic flow conditions, we believe that this can give insight into generic mechanisms related to drag reduction in presence of porous coating.

The DNS are performed in the computational domain $D = [-2, 8.24] \times [-2.56, 2.56] \times [-2.56, 2.56]$, previously used for the validation studies. The geometrical configuration is the one depicted in Fig. 1(b). According to the convergence study and the validation results reported in the previous section, the simulations at $Re = 300$ and $Re = 1000$ are carried out setting the grid resolution to $512 \times 256 \times 256$ ($h = 0.02$) and $1024 \times 512 \times 512$ ($h =$

0.01) respectively. The time step is adaptive and defined according to Eq. (8). As in the validation simulations, a perturbation is applied to the flow imposing $u_{y\infty} = a \sin(\pi(T - 3))$ between $T = 3$ and $T = 4$, with $a = 1$ at $Re = 300$ and $a = 0.1$ at $Re = 1000$.

In order to analyze the effects of our control approach, a comparison between the controlled devices and the uncontrolled obstacle is needed. For this purpose we will systematically analyze the following diagnostics in both cases:

- Global flow quantities:

- Aerodynamic force ($\mathcal{F} = (F_x, F_y, F_z)$): we consider drag and lift forces instead of drag and lift coefficients since the expressions of the latter involve the diameter d of the obstacle which is not clearly defined because of the porous coating. Indeed, when the permeability of the added porous layer tends to infinity, the obstacle tends to a hemisphere of smaller diameter.
- Enstrophy (Z): the enstrophy measures the dissipation effects in the flow. A decrease of enstrophy may lead in this context to a delay of transition to turbulence.

- (F_y, F_z) phase diagrams
- Time averaged and instantaneous vorticity fields.

4.1. Influence of the porous coating configuration and permeability on flow control efficiency

The passive control around the hemisphere is achieved by covering the obstacle with a porous coating for which different geometrical configurations are considered. These configurations are depicted in Fig. 3, where case 0 refers to the uncontrolled case (i.e. solid case), case 1 contains a porous layer on the whole hemisphere surface, case 2 involves two porous poles on top and bottom of the body, case 3 contains a porous zone corresponding to the rotation of the previous poles around the z -axis (this case will be denoted as “ring inlay” in the following) and case 4 implements an “annular coating”, consisting in a thin porous ring. Finally the “fluid case” corresponds to the hemisphere including a porous layer of infinite permeability ($\lambda = 0$): it actually represents a smaller hemisphere of diameter $d - 2\tau$ and thus a diminution of the Reynolds number. Here, the “fluid case” corresponds to a flow past a hemisphere of diameter $d = 0.8$ at $Re = 240$. This case has to be considered as a reference rather than a control device itself. It constitutes the lower limit of the control problem whereas the solid case (case 0) corresponds to the upper one.

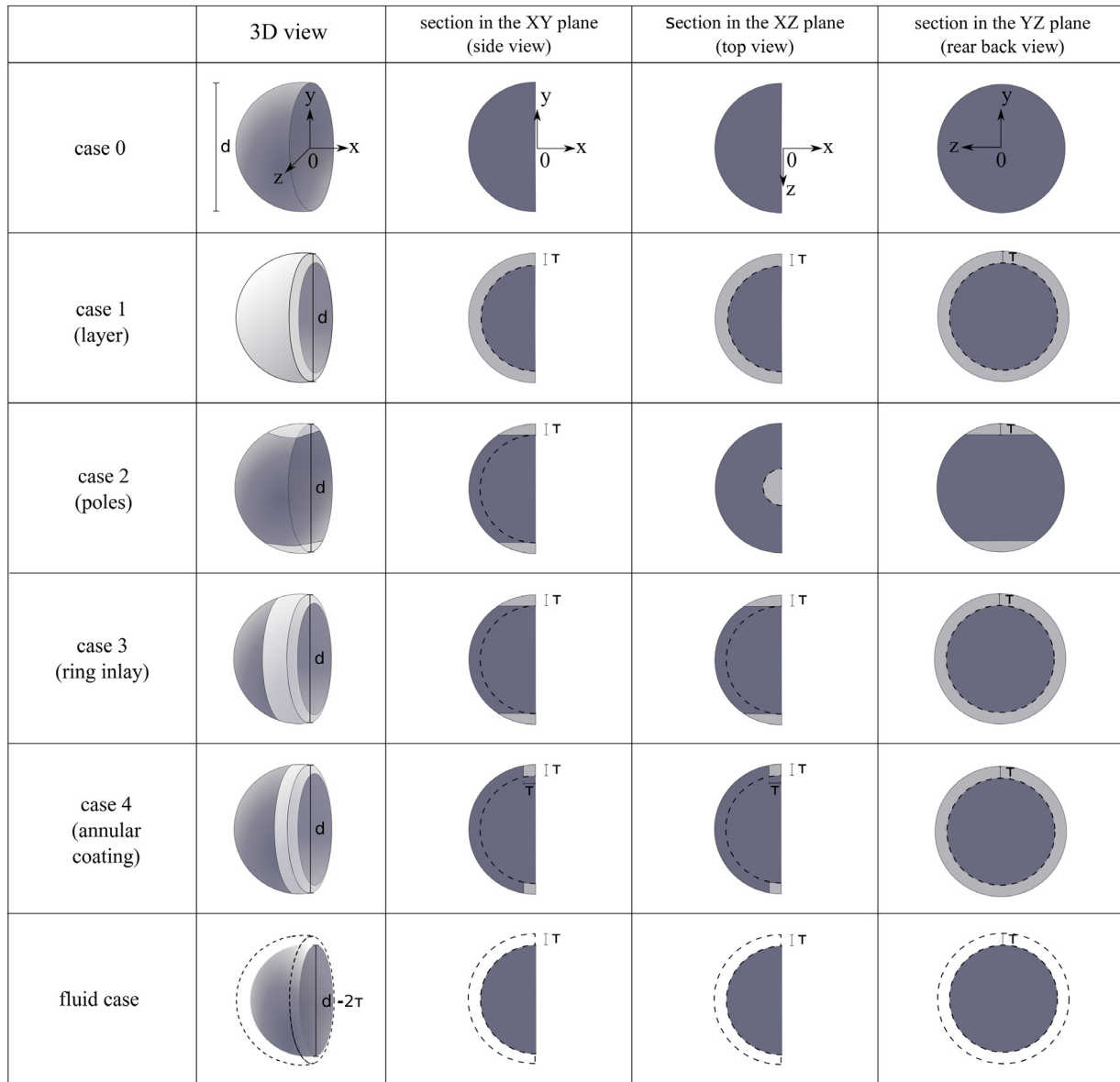


Fig. 3. Cases 1–4 corresponding to different porous layer configurations. Case 0 depicts the uncontrolled case and “fluid case” corresponds to the case of a smaller hemisphere of diameter $d - 2\tau$.

In the present simulations, all the solid parts of the hemisphere are modeled fixing $\lambda = 10^8$ and the porous areas of cases 1, 2, 3 and 4 will be modeled setting λ to 1 (very high permeability) or 10 (high permeability). When the non-dimensional λ value is equal to 1 and 10 it is equivalent to an intrinsic dimensional permeability in the order of $k = 10^{-3} \text{ m}^2$ and $k = 10^{-4} \text{ m}^2$, respectively. The choice of such values is based on the parametric studies performed by Bruneau & Mortazavi in [8], where those two λ values were found to give the best results in terms of drag and enstrophy reduction, and more recently by the present authors in [18], where a study was carried out in the two-dimensional case for a larger range of permeable λ values. The results showed that the most significant drag and enstrophy reductions were obtained for $1 \leq \lambda \leq 10$. Concerning the thickness τ of the coating, it is first set to 10% of the diameter ($\tau = 0.1$) for all the cases.

4.1.1. Numerical results for $Re = 300$

• $\lambda = 1$

The flow control results are first analyzed for $Re = 300$, fixing $\lambda = 1$ within the porous areas. At this regime, the less efficient

Table 3

Reduction effects brought by the different porous layer configurations in comparison to the uncontrolled case at $Re = 300$ with $\lambda = 1$ within the permeable regions and $\tau = 0.1$.

| $\lambda = 1, \tau = 0.1$ | \bar{F}_x | \bar{Z} |
|---------------------------|---------------|--------------|
| Case 0 | 0.285 | 73.0 |
| Case 1 (layer) | 0.246 (−14%) | 49.6 (−32%) |
| Case 2 (poles) | 0.269 (−7%) | 69.0 (−5.5%) |
| Case 3 (ring inlay) | 0.224 (−21%) | 55.0 (−25%) |
| Case 4 (annular coating) | 0.281 (−1.4%) | 73.3 (+0.4%) |
| Fluid case | 0.189 | 49.8 |

passive control device is the case 4. Indeed, as reported in Table 3 and Fig. 4, the drag reduction induced by the annular coating is particularly moderated (−1.4%) and concerning the enstrophy, one can notice a slight increase compared to the uncontrolled case (+0.4%).

The poor performance of this device is corroborated by Fig. 5, showing the time-averaged vorticity magnitude in the domain. On this figure one can indeed see that the mean wake obtained with case 4 is very similar to the one obtained with case 0. The

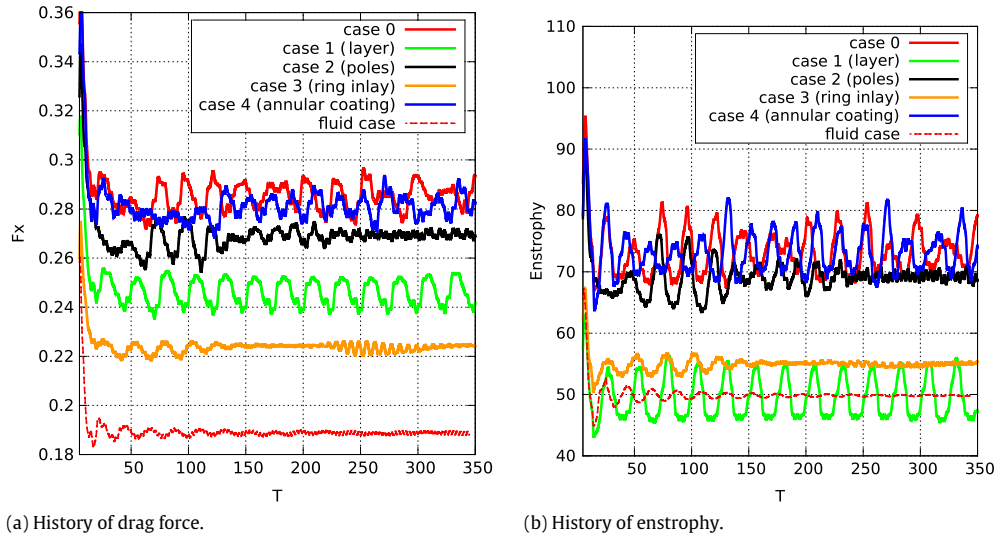
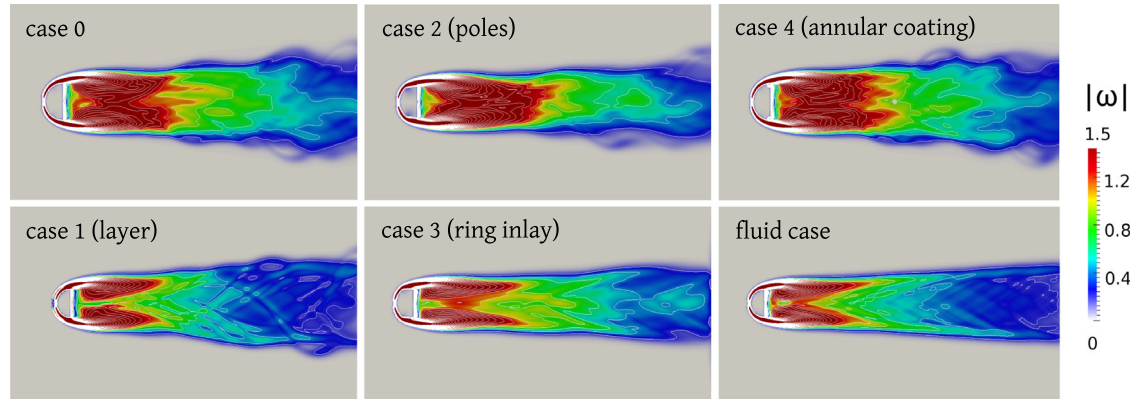
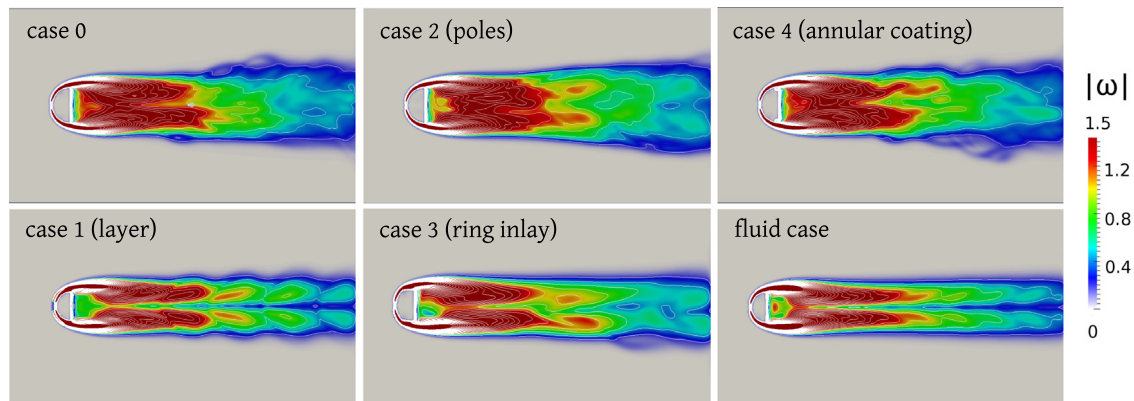


Fig. 4. Effects of various layer configurations on drag force (a) and enstrophy (b) for flow past a hemisphere at $Re = 300$, with $\lambda = 1$ within the permeable regions and $\tau = 0.1$.



(a) XY plane.



(b) XZ plane.

Fig. 5. Effects of various layer configurations on mean vorticity magnitude for flow past a hemisphere at $Re = 300$, with $\lambda = 1$ within the permeable regions and $\tau = 0.1$.

phase diagram (F_y , F_z) plotted in Fig. 6 also confirms that even with an annular coating, the flow remains chaotic and do not turn to become time-periodic. This statement is also verifiable with Fig. 4. The phase diagram related to case 4 is moreover very comparable to the one of the uncontrolled case (Fig. 6). Finally, the instantaneous 3D vorticity field $|\omega|$ of case 4, presented in Fig. 7, shows that the wake is thick and not planar symmetric. The lack of efficiency of this annular coating can be explained by the fact

that it is too close to the back wall edge and does not offer a clear entrance area for the upstream flow inside the porous part (see the side view and top view of case 4 in Fig. 3). This makes the adding of such device almost useless.

According to Table 3 and Fig. 4, the case 1 is an efficient device to reduce drag (-14%) and more especially enstrophy (-32%). The mean wake related to this type of controlled hemisphere is still relatively thick in the XY plane (although the vorticity intensity of

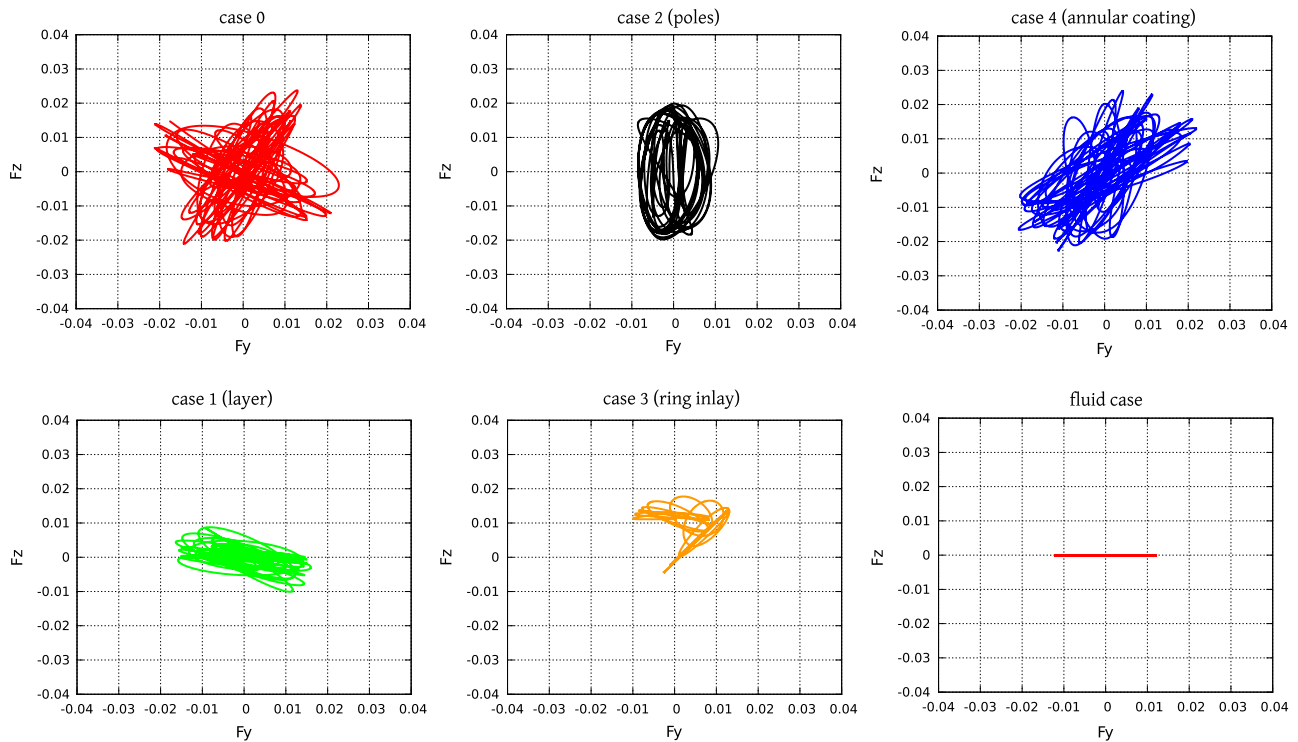


Fig. 6. Effects of various layer configurations on the phase diagram (F_y , F_z) for flow past a hemisphere at $Re = 300$, with $\lambda = 1$ within the permeable regions and $\tau = 0.1$.

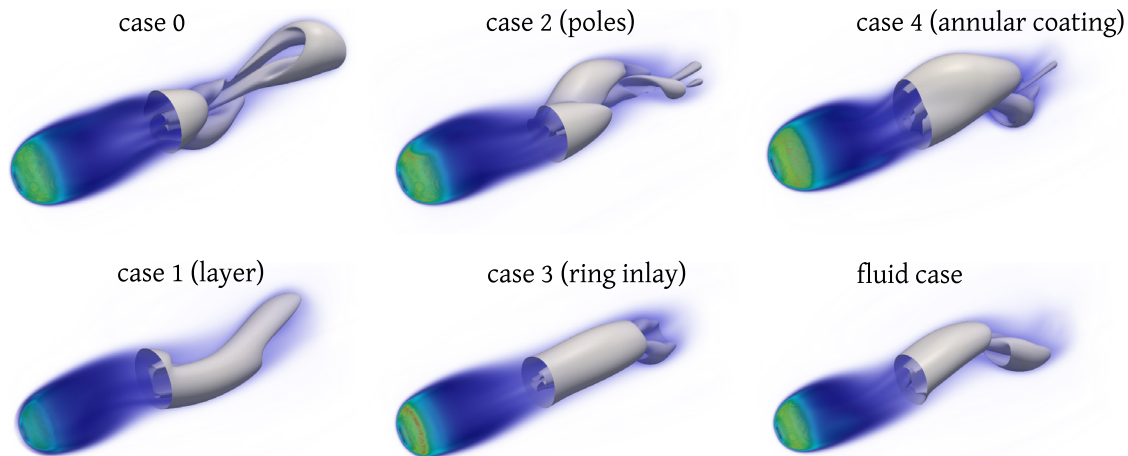


Fig. 7. Effects of various layer configurations on instantaneous vorticity magnitude 3D field and isocontour $|\omega| = 1$ for flow past a hemisphere at $Re = 300$, with $\lambda = 1$ within the permeable regions and $\tau = 0.1$.

the eddies is strongly decreased compared to case 0) but it shows a perfect symmetry in the XZ plane (Fig. 5). This planar symmetry is confirmed by Fig. 6 showing for case 1 a phase diagram centered around $F_z = 0$. This diagram also indicates an emerging time-periodicity in the solution which is indeed confirmed by Fig. 4. The representation of the 3D vorticity field in Fig. 7 clearly highlights the capability of the porous layer of case 1 to regularize the flow. We can notice that the result is very close to the one obtained with the fluid case, that is to say with the hemisphere of diameter $d - 2\tau = 0.8$, for which the actual Reynolds number is equal to 240, as mentioned previously. The efficiency of case 1 can be explained by the fact that the whole porous layer acts as a damper and regularizes the flow.

The results obtained with the case 2 are much less visible. Indeed, although the presence of porous poles tends to make the wake periodic (Fig. 6) and planar symmetric (Fig. 5(b)), high vorticity values can still be observed (Fig. 5), and finally the drag

force and the enstrophy only reduce respectively of 7% and 5.5% compared to the uncontrolled case (Table 3 and Fig. 4). The case 2 therefore has a positive effect but its action area remains too small compared to the whole separation zone.

Let us consequently focus on the case 3. The drag reduction induced by this type of device is the best one among all the considered configurations, with a diminution of 21%. As regards enstrophy, a decrease of 25% is observed with such a device (Table 3 and Fig. 4). These significant reductions are related to the global flow regularization, evidenced by the wake in Fig. 5 as well as the instantaneous vorticity in Fig. 7. Nevertheless, one can notice in Fig. 5(b) that with case 3 the phase is not planar symmetric, contrary to case 1. Indeed, the phase diagram (F_y , F_z) is not vertically centered at the point $F_z = 0$ (see Fig. 6). Furthermore, no clear periodic pattern emerges from the solution (see Fig. 4). Despite this absence of periodicity, we can however remark the low amplitude of the drag and enstrophy solution, which confirms

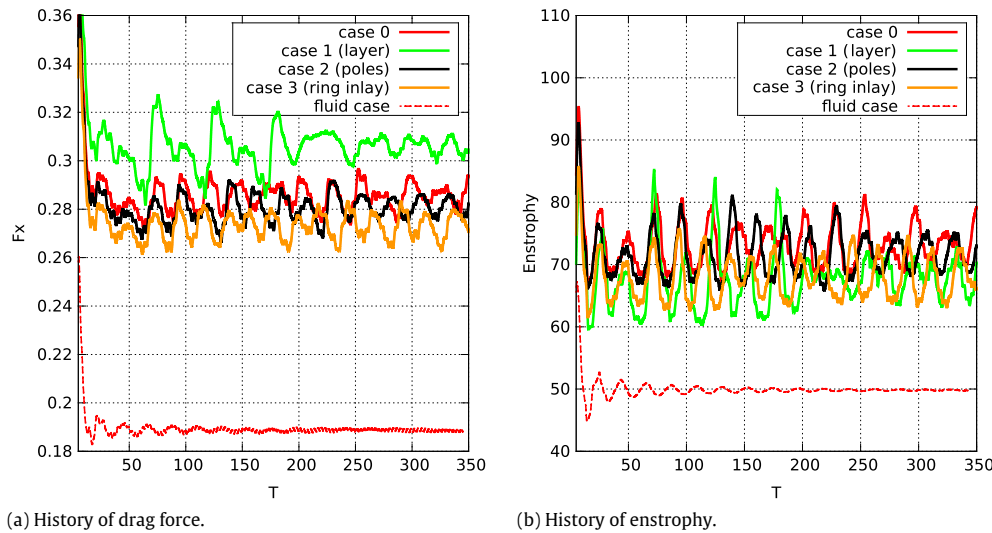


Fig. 8. Effects of various layer configurations on drag force (a) and enstrophy (b) for flow past a hemisphere at $Re = 300$, with $\lambda = 10$ within the permeable regions and $\tau = 0.1$.

the regularizing effects brought by this device. Unlike the case 4, the ring case 3 allows the flow to easily penetrate within the porous zone, leading to a great enhancement of the flow regularization.

Finally, in Fig. 6, the phase diagram of the fluid case indicates that with such a configuration the flow is time-periodic and planar symmetric (the diagram is a straight line on $F_z = 0$, perfectly centered around $F_y = 0$). Indeed, in this case smaller diameter results in a Reynolds number reduced to 240, and for this value the flow past a hemisphere was indeed shown in [38] to exhibit such properties.

These first results highlight the clear influence of the position of the porous coating around the hemisphere. In particular, the outcomes obtained with the case 3 show that the control efficiency in terms of drag reduction may be enhanced by only concentrating the porous areas in the vicinity of the flow separation zone. On the other hand, the complete porous layer (case 1) seems more competitive to achieve a global flow regularization, characterized here by the enstrophy value and the vorticity wake.

• $\lambda = 10$

In order to further investigate these hypotheses, the same devices are now analyzed at the same flow regime, considering a lower permeability within the porous areas, materialized by $\lambda = 10$. According to the previous discussion, the case 4 (i.e. the annular coating) will not be taken into consideration in this study and in the sequel.

In general, and as expected, the control performances obtained fixing $\lambda = 10$ in the porous areas are quite reduced compared to the one achieved with devices containing high permeable zones ($\lambda = 1$).

Concerning the case 1, the outcome is even more critical since one can notice non-beneficial effects in terms of drag production. Indeed, as shown by Table 4 and Fig. 8, case 1 is responsible for an increase of 7.4% of the drag force compared to the uncontrolled case. On the other hand, the case 1 allows an enstrophy reduction, although it is limited to -7% . Contrary to the results obtained with $\lambda = 1$ inside the porous layer of case 1, the mean wake is still rather perturbed here with $\lambda = 10$ (Fig. 9(a)) and do not present planar symmetry (Fig. 9(b)). The phase diagram of case 1 plotted in Fig. 10 is more regular than the one of case 0 but shows however non-negligible amplitudes for the lift forces F_y and F_z . In fact, decreasing the permeability makes the fluid displacement more difficult inside the front part of the porous layer. This increase of the resistance to the fluid movement in the boundary layer region is directly related to the rise of the drag force, which is

Table 4

Reduction effects brought by the different porous layer configurations in comparison to the uncontrolled case at $Re = 300$ with $\lambda = 10$ within the permeable regions and $\tau = 0.1$.

| $\lambda = 10, \tau = 0.1$ | \bar{F}_x | \bar{Z} |
|----------------------------|---------------|------------|
| Case 0 | 0.285 | 73.0 |
| Case 1 (layer) | 0.306 (+7.4%) | 67.7 (−7%) |
| Case 2 (poles) | 0.280 (−2%) | 71.5 (−2%) |
| Case 3 (ring inlay) | 0.273 (−4%) | 67.9 (−7%) |
| Fluid case | 0.189 | 49.8 |

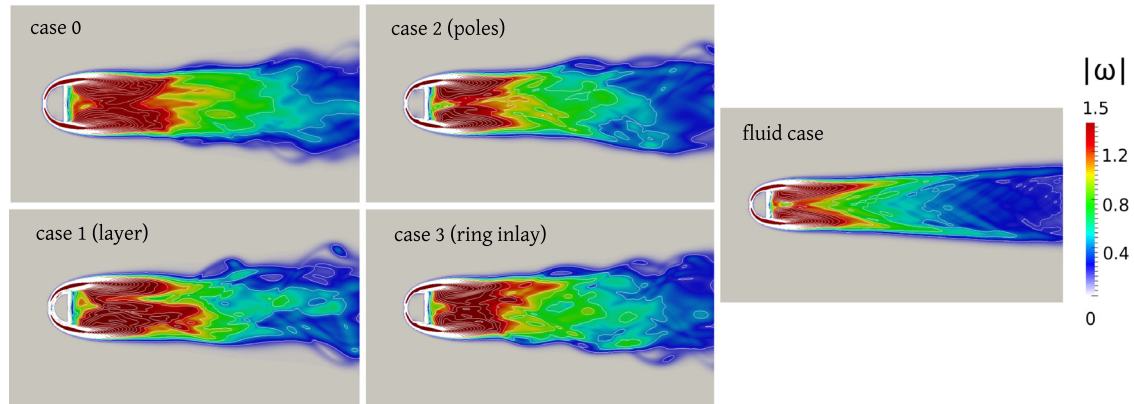
precisely a quantity evaluated on the walls of the obstacle. These results indicate the importance of the porous coating location for lower permeabilities. Once again it appears that, for drag reduction purpose, these areas should be concentrated in the vicinity of the flow separation points.

The results obtained with case 2 (permeable poles) confirm this statement. In this case, due to small concentrated porous surfaces the control effects are moderated (Table 4 and Fig. 8); however the performances are not deteriorated. From a qualitative point of view, the phase diagram (F_y, F_z) and the mean wake in the XY plane remain very similar to the one of case 0 (Figs. 10 and 9(a)), but a symmetry emerges in the XZ plane (Fig. 9(b)), confirming the beneficial effects brought by the two porous poles. The case 2 cannot be qualified as very efficient but in comparison with case 1 it can be assessed that the passive action in the vicinity of the back wall and shedding edge is important.

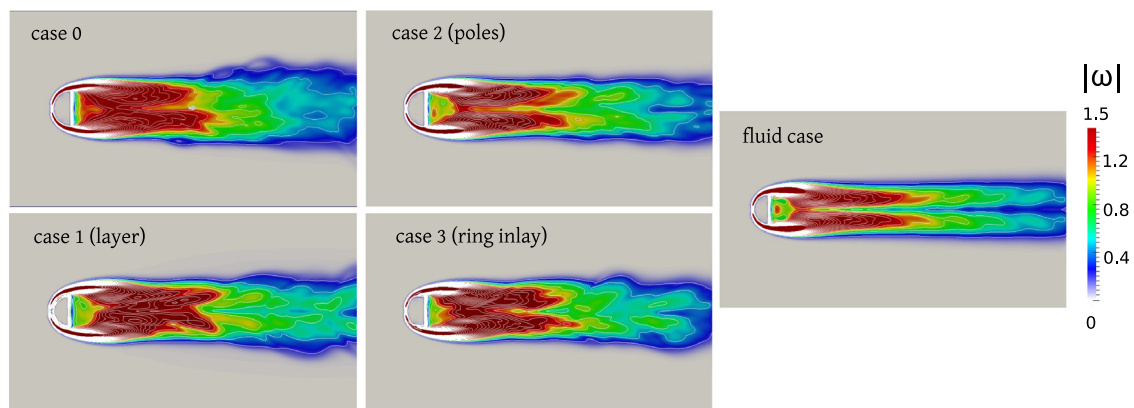
The best flow control device considered here is the case 3, allowing for a drag reduction of 4% and a decrease of the enstrophy of 7% (Table 4 and Fig. 8). Fig. 9(b) shows that compared to case 0 the flow better attaches to the obstacle with case 3, leading to a thinner wake. The 3D instantaneous vorticity fields depicted in Fig. 11 clearly show the benefits obtained with case 3 compared to cases 1 and 2 since its wake is the only one showing a clear regularization compared to case 0.

4.1.2. Numerical results for $Re = 1000$

Let us now focus on the flow control results at $Re = 1000$. At this regime, we only take into consideration the best configurations outlined in the previous section, namely the case 1 with $\lambda = 1$ within the porous layer, and the case 3 with $\lambda = 1$ and $\lambda = 10$ inside the porous ring. The reduction effects in terms of drag force and enstrophy are given by Table 5 and Fig. 12. As can be seen, the case 3 with $\lambda = 1$ is the only device providing a drag decrease



(a) XY plane.



(b) XZ plane.

Fig. 9. Effects of various layer configurations on mean vorticity magnitude for flow past a hemisphere at $Re = 300$, with $\lambda = 10$ within the permeable regions and $\tau = 0.1$.

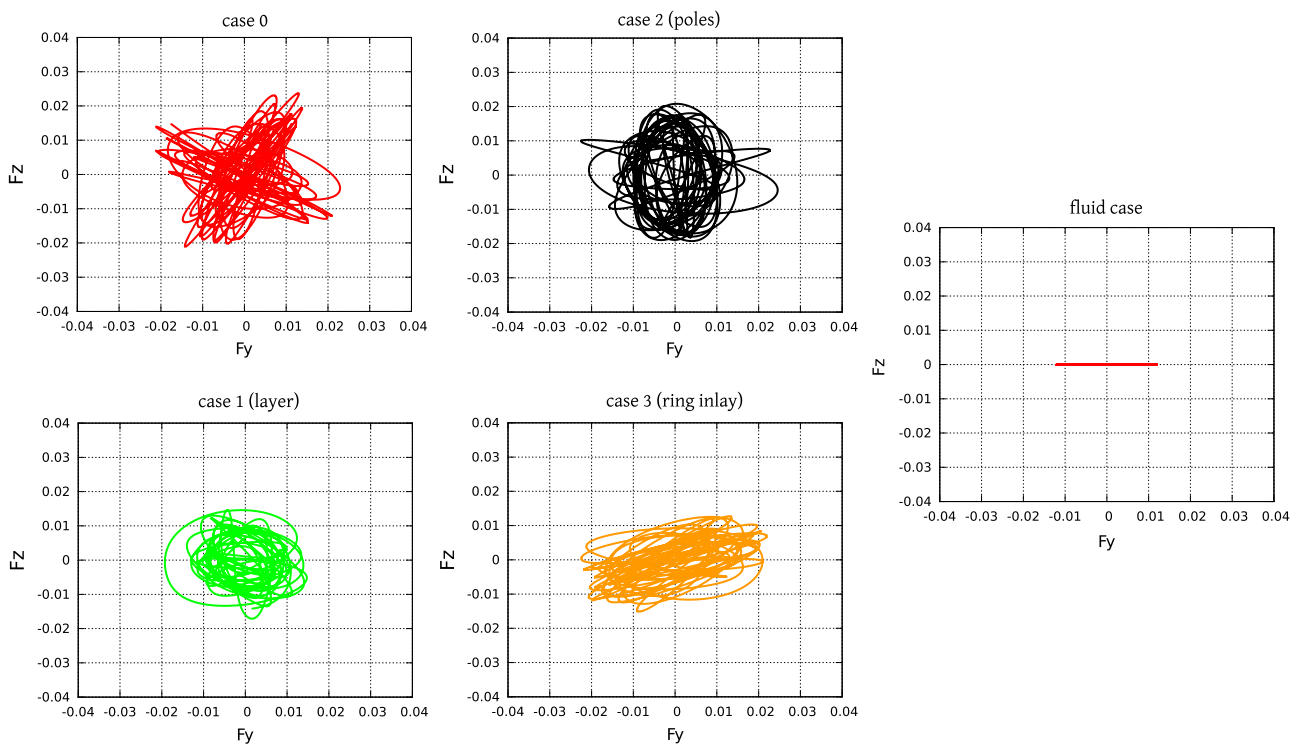


Fig. 10. Effects of various layer configurations on the phase diagram (F_y, F_z) for flow past a hemisphere at $Re = 300$, with $\lambda = 10$ within the permeable regions and $\tau = 0.1$.

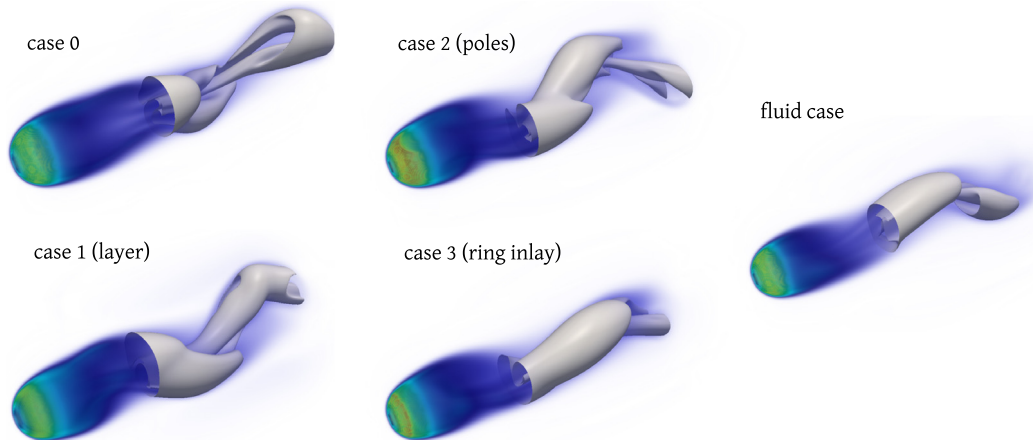


Fig. 11. Effects of various layer configurations on instantaneous vorticity magnitude 3D field and isocontour $|\omega| = 1$ for flow past a hemisphere at $Re = 300$, with $\lambda = 10$ within the permeable regions and $\tau = 0.1$.

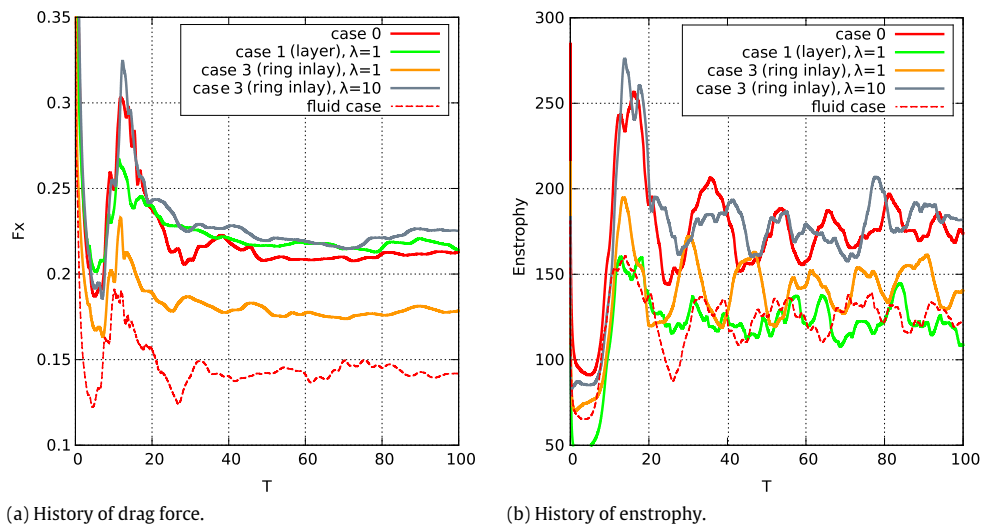


Fig. 12. Effects of various layer configurations on drag force (a) and entrophy (b) for flow past a hemisphere at $Re = 1000$, with $\tau = 0.1$.

(−16%). In particular, case 1 with $\lambda = 1$ is responsible for a drag increase of 3% while it ensures a reduction of entrophy of 30%, which is more than the reduction achieved with case 3 and $\lambda = 1$ (−19%). As observed at $Re = 300$, the case 1 is better suited to regularize the wake. Indeed, as can be noticed on Fig. 13, the porous layer of permeability $\lambda = 1$ significantly impacts the wake that tends to present the same characteristics that the one of the fluid case. It allows in particular to recover a planar symmetric wake (Fig. 13(b)), which is not the case for the case 3 with $\lambda = 1$. However, the latter represents the best device in terms of overall regularization. Besides the important reductions reported in Table 5, the mean wake obtained from case 3 with $\lambda = 1$ is smoother than the one of case 0, with lower vorticity values and a thinner dimension in the crosswise direction (Fig. 13(a)) and in the spanwise direction (Fig. 13(b)). The instantaneous 3D vorticity field depicted in Fig. 14 also shows the same effects on the wake and enhances the regularization capabilities of such device. On the contrary, setting $\lambda = 10$ within the porous area of case 3 deteriorates the performances. The wake indeed thickens, showing higher vorticity values (Figs. 13 and 14), and the drag force as well as the entrophy raise of 5% and 2% respectively (Table 5 and Fig. 12). Therefore, among the configurations handled in this flow control study at $Re = 1000$ with the layer thickness $\tau = 0.1$, the most competitive device is clearly the case 3 with a high permeability ($\lambda = 1$) settled within the porous coating.

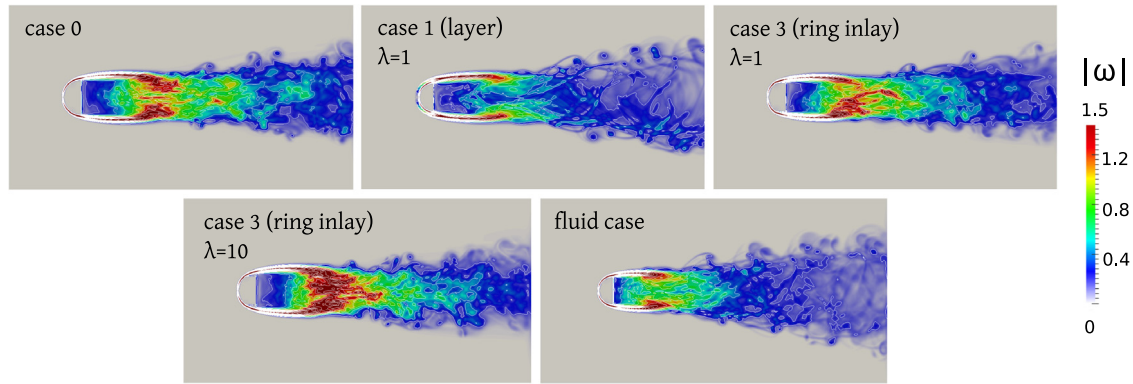
Let us discuss the results obtained in this section. In terms of control efficiency and especially drag reduction, the main

Table 5

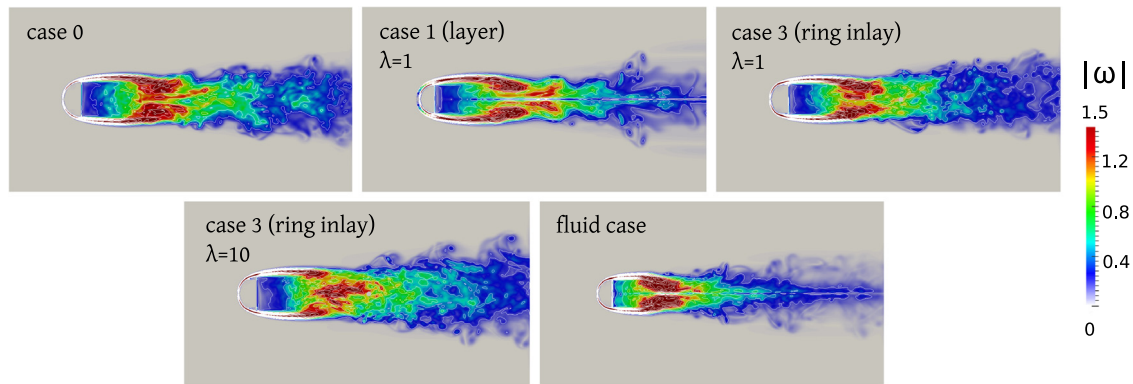
Reduction effects brought by different porous layer configurations in comparison to the uncontrolled case at $Re = 1000$ with $\tau = 0.1$.

| $\tau = 0.1$ | \bar{F}_x | \bar{Z} |
|-------------------------------------|--------------|--------------|
| Case 0 | 0.210 | 175.8 |
| Case 1 (layer), $\lambda = 1$ | 0.217 (+3%) | 123.1 (−30%) |
| Case 3 (ring inlay), $\lambda = 1$ | 0.177 (−16%) | 141.8 (−19%) |
| Case 3 (ring inlay), $\lambda = 10$ | 0.221 (+5%) | 179.6 (+2%) |
| Fluid case | 0.143 | 126.5 |

outcome is the necessity for the Darcy velocity to settle within the porous medium before reaching the detachment point. However, we observed that the presence of an homogeneous porous layer around the obstacle implied flow resistance in the upstream region (case 1). The solution retained in this study is therefore the one where the porous zones are concentrated in the vicinity of the separation line, avoiding the flow to be damped by the porous layer but modifying the shedding with a pressure rise on the back wall (case 3). From a qualitative point of view, it is interesting to note that these results are in good agreement with the experimental studies carried out by Ruck et al. [39] where different porous sheaths made of polyester foam are added to the surface of a circular cylinder in order to decrease the drag force. Indeed, despite the different flow regimes considered in their study (in their case the Reynolds number ranges from 10^4 to $1.3 \cdot 10^5$), the authors



(a) XY plane.



(b) XZ plane.

Fig. 13. Effects of various layer configurations on mean vorticity magnitude for flow past a hemisphere at $Re = 1000$, with $\tau = 0.1$.

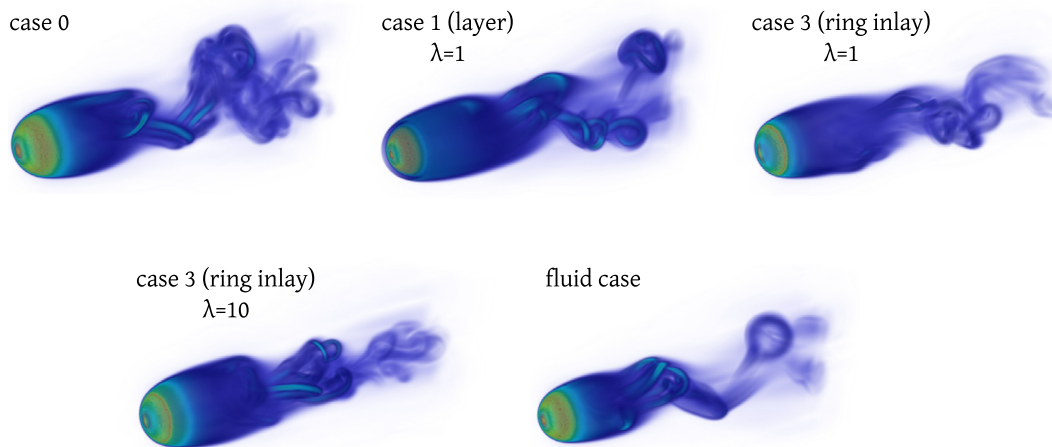


Fig. 14. Effects of various layer configurations on instantaneous vorticity magnitude 3D field for flow past a hemisphere at $Re = 1000$, with $\tau = 0.1$.

also found that a fully porous surface deteriorates the aerodynamic performances whereas partially coated surfaces, precisely located in the leeward side of the cylinder, lead to a drag reduction.

An other important observation that emerges from this parametric study is the difference of behavior between the enstrophy and the drag evolution, depending on the controlled cases. With a porous layer covering the whole hemisphere front surface (case 1), we indeed highlighted a systematic enstrophy reduction compared to the uncontrolled case, regardless of the permeability and the Reynolds number, whereas some values of λ were found to be responsible for a non negligible drag increase. As evoked previously, this is directly due to the way these two quantities are eval-

uated. The enstrophy quantifies the energy dissipation of the system in the whole domain. Thus, the laminar velocities caused by the presence of the large permeable layer lead to a delay in transition to turbulence and directly impact the transport of the vorticity which is regularized. On the contrary, the drag force is evaluated on the boundaries of the obstacle or in the vicinity of the body and is directly linked to the vorticity generation. Therefore, the friction phenomenon caused by lower permeabilities of the porous layer ($\lambda = 10$) and implying a resistance to the flow in the front part of the obstacle, is directly reported in the drag diagnostic and in the very near-wake analysis.

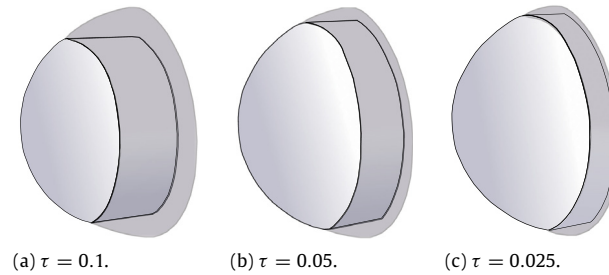


Fig. 15. Graphical representation of the control device corresponding to case 3 (ring inlay). Three different thicknesses τ are considered. The shaded transparent areas depict the permeable part of the hemisphere.

Table 6

Reduction effects brought by the case 3 (ring inlay) configuration with $\lambda = 1$ within the permeable region, in comparison to the uncontrolled case at $Re = 1000$.

| $\lambda = 1$ | \bar{F}_x | \bar{Z} |
|------------------------|--------------|--------------|
| Case 0 | 0.210 | 175.8 |
| Case 3, $\tau = 0.1$ | 0.177 (−16%) | 141.8 (−19%) |
| Case 3, $\tau = 0.05$ | 0.198 (−6%) | 170.6 (−3%) |
| Case 3, $\tau = 0.025$ | 0.201 (−4%) | 170.4 (−3%) |

4.2. Influence of the porous layer thickness τ on flow control efficiency

In this section we focus on the influence of the porous coating thickness τ on the flow control efficiency. This study is performed at $Re = 1000$ using the ring inlay device (case 3) with a $\lambda = 1$ permeability. These choices restrict the study to the best parameters for the highest Reynolds number in this work. Indeed, according to the above discussion, this device appears as a good compromise between flow control efficiency and manufacturing constraints since it presents good performances while involving a few quantity of porous material. Naturally, in order to push further this investigation, it is interesting to verify the performances of such a device with a thickness lower than $\tau = 0.1$. We consider for that purpose two other values of τ , namely $\tau = 0.05$ and $\tau = 0.025$. The 3D representation of the ring inlay device (case 3) with the different values of τ is given by Fig. 15.

Table 6, Figs. 16 and 17 show a non-linear decrease of drag and enstrophy as the porous ring inlay thickens. Indeed, the drag and enstrophy reductions obtained with $\tau = 0.05$ and 0.025 are noticeably tempered compared to the case where $\tau = 0.1$ and similar to each other. The regularization effects brought by the cases $\tau = 0.05$ and $\tau = 0.025$ are also qualitatively reported in Figs. 18 and 19. They show that the mean and instantaneous wakes obtained with $\tau = 0.025$ in case 3 resemble to the one obtained with the uncontrolled case. A smoothing tendency is then observed from this lower value of τ to the higher one. At this flow regime, the ring inlay configuration (case 3) with $\tau = 0.1$ therefore appears as the most suitable control device. However, this value of $\tau = 0.1$ corresponds to a rather thick porous coating around the obstacle (Fig. 15(a)). Therefore, in terms of effectiveness, the ring inlay configuration with $\tau = 0.05$ could be considered as a good compromise since it needs a very low quantity of porous material while allowing a non negligible drag reduction (−6%).

5. Conclusion

In this work, a three-dimensional vortex-penalization method was proposed in order to easily handle solid–fluid–porous media. The differentiation between the three different media is indeed performed defining the value of the penalization parameter in the Brinkman–Navier–Stokes equations without prescribing a boundary condition at the solid boundary or a condition at the porous–fluid interface. The method was validated for transitional flows around a sphere and a hemisphere with grid convergence

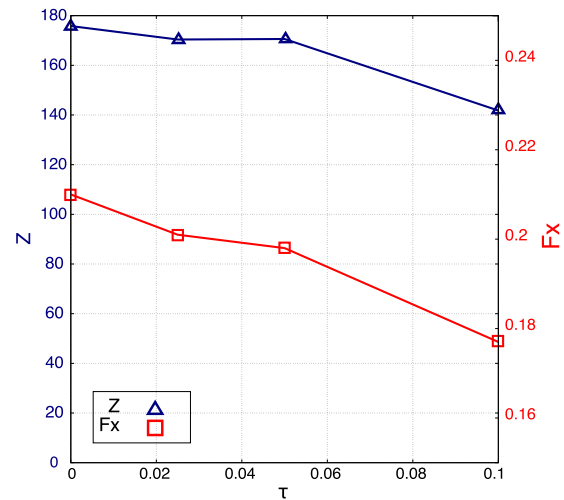


Fig. 16. Figure associated to Table 6 (enstrophy is represented by the blue-triangled line and the drag force by the red-squared line). (For interpretation of the references to color in this figure legend, the reader is referred to the web version of this article.)

evaluations and comparisons to the literature. This validation study showed the capabilities of the present approach to accurately model flows past different types of bluff bodies.

In the second part of the paper, the method was applied to the design of passive control strategies for flow past a hemisphere at $Re = 300$ and $Re = 1000$, consisting in adding porous coatings on the obstacle surface in order to smooth the flow dynamics. The presence of a porous zone at the solid–fluid interface is indeed responsible for a decrease of the shear forces and the vorticity generation at the boundary layer, thus enabling wake stabilization and drag reduction. From this flow control study, it turns out that the drag force is rather sensitive to the permeability of the added porous coating and that the location of the latter has a real impact on the drag reduction. Among the control devices investigated in this work, one can retain the “ring inlay” configuration which only includes porous parts in the region of the flow separation. With an appropriate choice of the permeability and the thickness, this porous device represents a good compromise between control efficiency and manufacturing constraints. Ongoing work consists in extending the present study to higher Reynolds numbers using turbulence models.

In this paper we have considered control parameters that have axial symmetry. One may generalize this approach to control strategies which would consist in porous coatings with variations in the azimuthal direction. In [40] this technique has been used with success in combination with active control of a cylinder wake, with significant improvements over axisymmetric optimal control strategies. Future works will therefore deal with a stability analysis at transitional Reynolds numbers of the uncontrolled flow. This analysis will help determining and reinforcing the physical mechanisms responsible for the beneficial effects brought by the control.

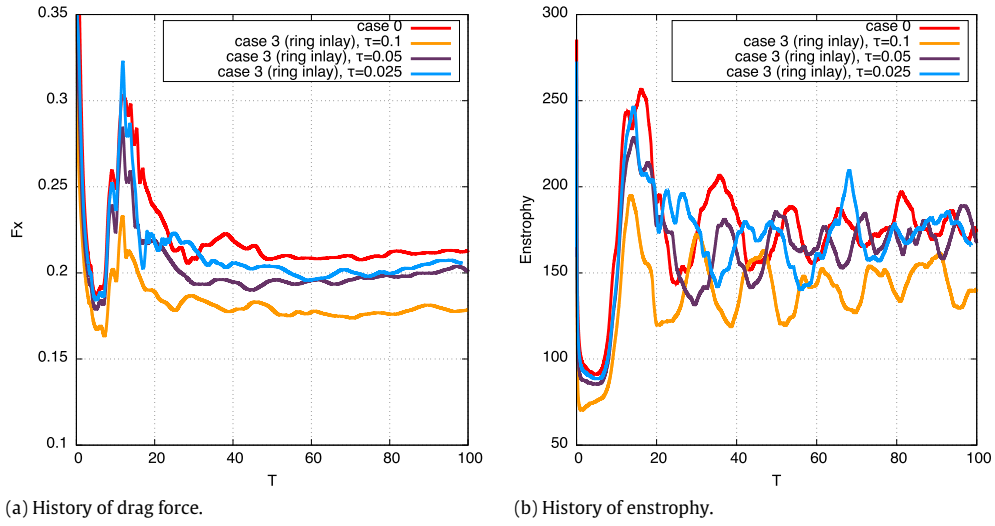


Fig. 17. Effects of various layer thicknesses τ for case 3 on drag force (a) and enstrophy (b) for flow past a hemisphere at $Re = 1000$, with $\lambda = 1$ within the permeable region.

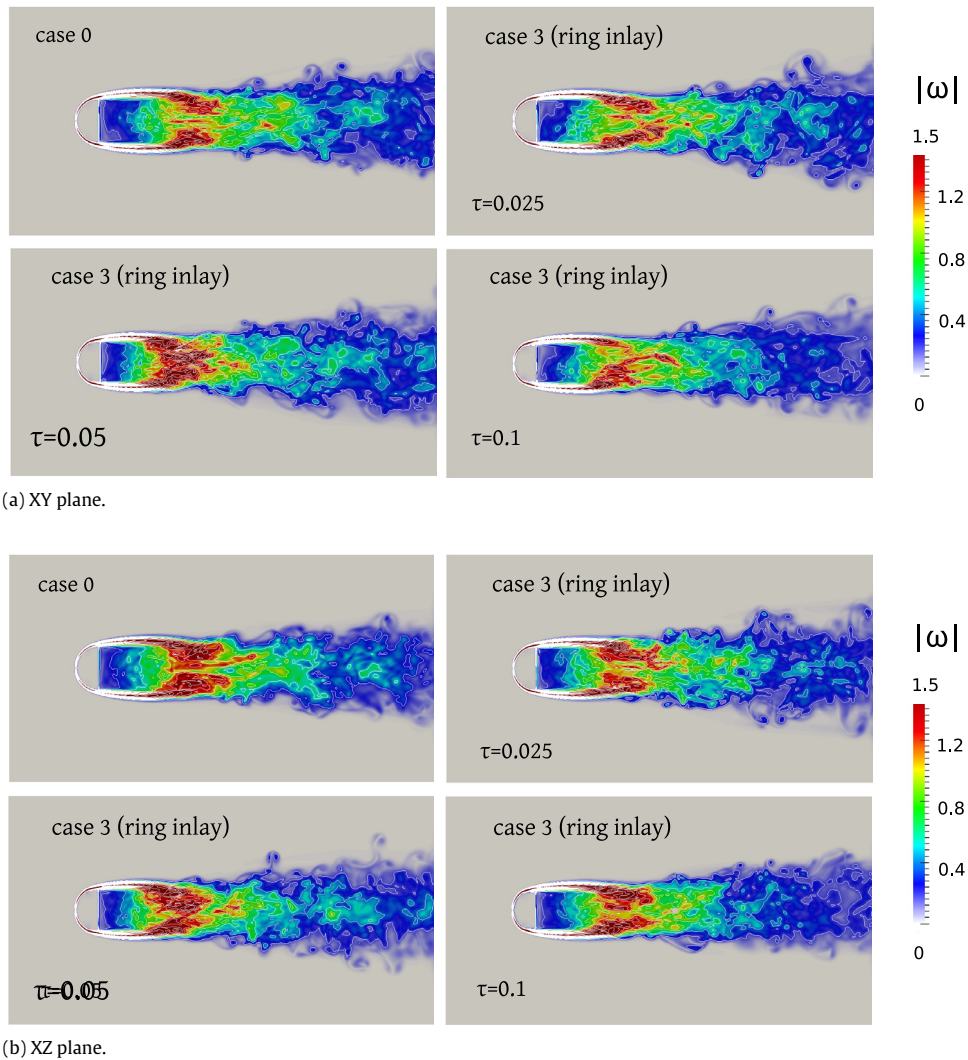


Fig. 18. Effects of various layer thicknesses τ for case 3 on mean vorticity magnitude for flow past a hemisphere at $Re = 1000$, with $\lambda = 1$ within the permeable region.

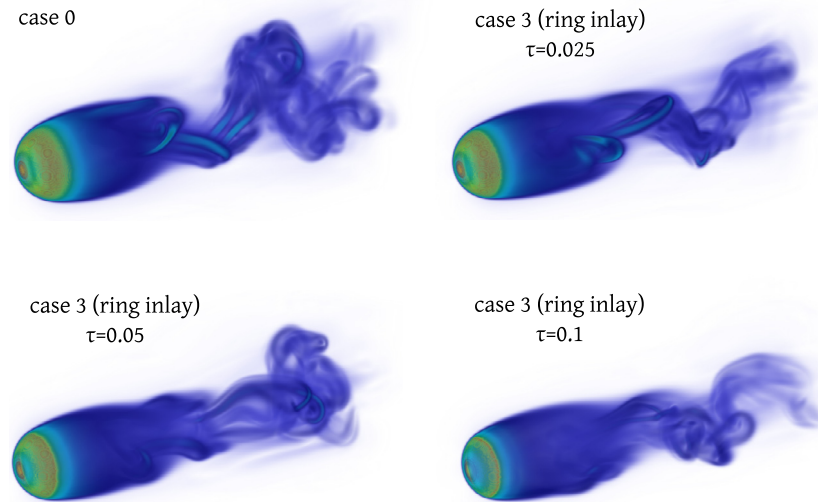


Fig. 19. Effects of various thicknesses τ for case 3 on instantaneous vorticity magnitude 3D field for flow past a hemisphere at $Re = 1000$, with $\lambda = 1$ within the permeable region.

Acknowledgment

The authors wish to thank Rajat Mittal for helpful discussions.

References

- [1] O. Wiplier, U. Ehrenstein, Numerical simulation of linear and nonlinear disturbance evolution in a boundary layer with compliant walls, *J. Fluids Struct.* 14 (2) (2000) 157–182.
- [2] C. Davies, P. Carpenter, Instabilities in a plane channel flow between compliant walls, *J. Fluid Mech.* 352 (1997) 205–243.
- [3] U. Ehrenstein, On the linear stabilities of channel flow over riblets, *Phys. Fluids* 8 (1996) 3194.
- [4] P. Luchini, Asymptotic analysis of laminar boundary-layer flow over finely grooved surfaces, *Eur. J. Mech. B Fluids* 14 (2) (1995).
- [5] P. Bearman, M. Branković, Experimental studies of passive control of vortex-induced vibration, *Eur. J. Mech. B Fluids* 23 (2004) 9–15.
- [6] M. Zdravkovich, Review and classification of various aerodynamic and hydrodynamic means for suppressing vortex shedding, *J. Wind Eng. Ind. Aerodyn.* 7 (2) (1981) 145–189.
- [7] H. Wong, A means of controlling bluff body separation, *J. Ind. Aerodyn.* 4 (2) (1979) 183–201.
- [8] C.-H. Bruneau, I. Mortazavi, Passive control of the flow around a square cylinder using porous media, *Internat. J. Numer. Methods Fluids* 46 (2004) 415–433.
- [9] Y. Achdou, O. Pironneau, F. Valentin, Effective boundary conditions for laminar flows over periodic rough boundaries, *J. Comput. Phys.* 147 (1998) 187–218.
- [10] F. Pluvinage, A. Kourta, A. Bottaro, Instabilities in the boundary layer over a permeable, compliant wall, *Phys. Fluids* 26 (2014).
- [11] R. Mehta, J.M. Pallsi, The aerodynamics of a tennis ball, *Sports Eng.* 4 (4) (2001) 177–189.
- [12] A. Vaseashta, D. Dimova-Malinovska, Nanostructured and nanoscale devices, sensors and detectors, *Sci. Technol. Adv. Mater.* 6 (2005) 312–318.
- [13] F. Gosselin, Mécanismes d'interactions fluide-structure entre écoulements et végétation (Ph.D. thesis), Ecole Polytechnique, Palaiseau, France, 2009.
- [14] D. Venkataraman, A. Bottaro, Numerical modeling of flow control on a symmetric aerofoil via a porous compliant coating, *Phys. Fluids* 24 (2012) 093601.
- [15] T. Secomb, R. Hsu, A. Pries, Effect of the endothelial surface layer on transmission of fluid shear stress to endothelial cells, *Biorheology* 38 (2001) 143–150.
- [16] C.-H. Bruneau, I. Mortazavi, Control of vortex shedding around a pipe section using a porous sheat, *J. Offshore Polar Eng.* 16 (2006).
- [17] C.-H. Bruneau, P. Gilliéron, I. Mortazavi, Passive control around a two-dimensional square back ahmed body using porous media, *J. Fluids Eng.* 130 (6) (2008).
- [18] C. Mimeau, I. Mortazavi, G.-H. Cottet, Passive flow control around a semi-circular cylinder using porous coatings, *Int. J. Flow Control* 6 (2014) 43–60.
- [19] G.-H. Cottet, P. Koumoutsakos, *Vortex Methods - Theory and Practice*, Cambridge University Press, 2000.
- [20] P. Koumoutsakos, A. Leonard, High-resolution simulations of the flow around an impulsively started cylinder using vortex methods, *J. Fluid Mech.* 296 (1995) 1–38.
- [21] J.P. Caltagirone, Sur l'interaction fluide-milieu poreux: Application au calcul des efforts exercés sur un obstacle par un fluide visqueux, *C. R. Acad. Sci. Paris* 318 (1994).
- [22] P. Angot, C.-H. Bruneau, P. Fabrie, A penalization method to take into account obstacles in incompressible viscous flows, *Numer. Math.* 81 (1999) 497–520.
- [23] N. Kevlahan, J.M. Ghidaglia, Computation of turbulent flow past an array of cylinders using a spectral method with Brinkman penalization, *Eur. J. Mech. B/Fluids* 20 (2001) 333–350.
- [24] A.J. Chorin, Numerical study of slightly viscous flow, *J. Fluid Mech.* 57 (1973) 785–796.
- [25] M. Bergdorf, P. Koumoutsakos, A Lagrangian particle-wavelet method, *SIAM Multiscale Model. Simul.* 5 (2006) 980–995.
- [26] G.-H. Cottet, J.-M. Etancelin, F. Perrignon, C. Picard, High order semi-lagrangian particles for transport equations: numerical analysis and implementation issues, *ESAIM Math. Model. Numer. Anal.* 48 (2014) 1029–1064.
- [27] C. Mimeau, G.-H. Cottet, I. Mortazavi, Direct numerical simulation of 3D bluff-body flows by a vortex penalization method, *Comput. Fluids* 136 (2015) 331–347.
- [28] C. Mimeau, F. Gallizio, G.-H. Cottet, I. Mortazavi, Vortex penalization method for bluff body flows, *Internat. J. Numer. Methods Fluids* 79 (2015) 55–83.
- [29] F.W. Roos, W.W. Willmarth, Some experimental results on sphere and disk drag, *AIAA J.* 9 (1971) 285–291.
- [30] T.A. Johnson, V.C. Patel, Flow past a sphere up to a Reynolds number of 300, *J. Fluid Mech.* 378 (1999) 19–70.
- [31] A. Tomboulides, A. Orszag, Numerical investigation of transitional and weak turbulent flow past a sphere, *J. Fluid Mech.* 416 (2000) 45–73.
- [32] G.S. Constantinescu, K.D. Squires, LES and DES investigations of turbulent flow over a sphere., *AIAA Paper 2000-0540*, 2000.
- [33] D. Kim, H. Choi, Laminar flow past a sphere rotating in the streamwise direction, *J. Fluid Mech.* 461 (2002) 365–386.
- [34] P. Ploumhans, G.S. Winckelmans, J.K. Salmon, A. Leonard, M.S. Warren, Vortex methods for direct numerical simulation of three-dimensional bluff body flows: Applications to the sphere at $Re = 300, 500$ and 1000 , *J. Comput. Phys.* 178 (2002) 427–463.
- [35] J. Wu, G. Faeth, Sphere wakes in still surroundings at intermediate Reynolds numbers, *AIAA J.* 31 (8) (1993) 1448–1455.
- [36] E. Poon, G. Iaccarino, A. Ooi, M. Giacobello, Numerical studies of high Reynolds number flow past a stationary and rotating sphere, in: *Seventh International Conference on CFD in the Minerals and Process Industries CSIRO*, Melbourne, Australia, 2009.
- [37] R. Campregher, J. Militzer, S. Mansur, A. da Silveira Neto, Computations of the flow past a still sphere at moderate Reynolds numbers using an immersed boundary method, *J. Braz. Soc. Mech. Sci. Eng.* 31 (4) (2009) 344–352.
- [38] D. Kim, H. Choi, Laminar flow past a hemisphere, *Phys. Fluids* 15 (8) (2003) 2457–2460.
- [39] B. Ruck, K. Klausmann, T. WackerRussell, The flow around circular cylinders partially coated with porous media, *AIP Conf. Proc.* 1453 (2012) 49–54.
- [40] P. Poncet, R. Hildebrand, G.-H. Cottet, P. Koumoutsakos, Spatially distributed control for optimal drag reduction of the flow past a circular cylinder, *J. Fluid Mech.* 599 (2008) 111–120.